Published in "Journal of Sol-Gel Science and Technology 95(3): 719–732, 2020"
which should be cited to refer to this work.

Monolithic resorcinol–formaldehyde alcogels and their corresponding nitrogen-doped activated carbons

Abstract

Here we report the adaptation of formaldehyde crosslinked phenolic resin-based aerogel and xerogel synthesis to ethanol-based solvent systems. Three specific formulations, namely one resorcinol–formaldehyde (RF) and two resorcinol–melamine–formaldehyde (RMF) systems were studied. As-prepared resins were characterized in terms of envelope and skeletal density. Furthermore, resin samples were pyrolyzed and activated in a CO_2 gas atmosphere using a single-step protocol. The corresponding carbon materials featured high surface areas, moderate water uptake capacity and thermal conductivities in the 0.1 $W.m^{-1}K^{-1}$ range, in line with comparable activated carbons. The amount of formaldehyde in the synthesis of the RMF derived carbons proved to be a critical parameter in terms of both structural features and amount of N dopant in the carbonaceous matrix. Furthermore, a high formaldehyde concentration also has a drastic effect on the pore structure of the corresponding RMF carbons, leading primarily to mesopore formation without almost any macropore formation. Perhaps more importantly, the effect of the ammonia curing catalyst concentration on the material microstructure showed the opposite effect as observed in classical, water-based phenolic resin preparations. The ethanol-based synthesis clearly affects the pore structure of the resulting materials but also opens up the possibility to create inorganic/organic hybrid materials by simple combination with classical alkoxide-based silica sol–gel chemistry.

Graphical Abstract

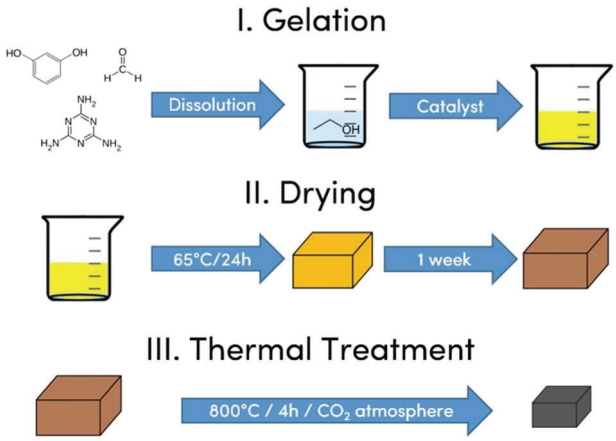

Supplementary information

✉ Romain Civioc
romain.civioc@empa.ch

[1] Empa, Swiss Federal Laboratories for Materials Science and Technology, Ueberlandstrasse 129, 8600 Duebendorf, Switzerland

[2] Department of Chemistry, University of Fribourg, Chemin du Musée 9, 1700 Fribourg, Switzerland

Keywords Phenolic resin · Activated carbon · Aerogel · Monolithic · Adsorption · N-doping

Highlights

- Transposition of a porous phenolic resin recipe from an aqueous to an ethanolic environment.
- Improvement of Nitrogen retention rate through pyrolysis and activation.
- One-step combined heat treatment to create microporosity.
- Compatibilization with inorganic systems such as alkoxysilanes.
- Results differ from current literature in some way.

1 Introduction

Porous materials come in a wide array of shapes and functionalities. Amongst them are activated carbons, materials consisting of a porous carbonaceous structure typically obtained by the pyrolysis and activation of organic precursors. Those can be either sourced directly from biomass [1–3] or synthesized by means of condensation of organic compounds such as the archetypal resorcinol–formaldehyde (RF) resin systems which were first reported by Pekala in 1989 [4]. Such sol–gel synthetic routes are highly tailorable, allowing for a controlled doping with heteroatoms such as sulfur [5], phosphorus [6], fluorine [7], boron [8], and most prominently nitrogen. Comprehensive overviews can be found elsewhere in the literature [6, 9]. Here we focus on nitrogen-doped carbon materials. N-doping is typically achieved by the use of a nitrogen-bearing co-precursor such as melamine [10–12], forming so-called RMF (Resorcinol–Melamine–Formaldehyde) resins. These porous networks can then be pyrolyzed and optionally activated, yielding the corresponding (activated) carbon materials. The microporosity arising from the activation step further accentuates their hierarchical microstructure that makes them excellent candidates for adsorption applications, thanks to their high water uptake potential. In fact, previous in-house work has shown that carbons resulting from pyrolyzed and activated RF resins are indeed suitable candidates as sorbents for adsorption heat pumps, especially when doped with nitrogen [13]. N-doping shifts the water isotherm towards adsorption at lower relative humidities while retaining other properties of the original material such as its envelope density and its thermal conductivity. The result is a material displaying a good compromise between heat and vapor transport as well as water sorption properties.

One major restriction with these materials is their incompatibility with inorganic Sol–Gel materials such alkoxysilane based silica gels, which would open new possibilities for creating new hybrid silica-organic or silica-carbon materials if it were overcome. Most publications on RF systems similar to Pekala's in the literature are water-based and there are only very few reports employing organic solvent systems such as isopropanol [14], methanol [15], or ethanol with the aid of a triblock copolymer as a template [16]. An ethanol-based recipe would be highly desirable because of a much easier post-processing of the gels (no need for solvent exchange prior to supercritical drying) and compatibility with the silica-based sol–gel chemistry mentioned above. To this end, a small amount of water (regardless of whether it is added or is formed during gelation) does not present a problem for neither the supercritical drying nor the compatibility with the silica chemistry. In fact, the standard synthesis of the latter already includes some water as means of a controlled partial hydrolysis [17].

In this study, we report the adaptation of the aforementioned RF phenolic resin chemistry to an alcohol-based recipe with essentially water-free starting conditions, as well as a nitrogen-doped RF (RMF) recipe. The recipe cannot, however, be categorized as anhydrous because of the stoichiometric release of water during polycondensation reactions that occur throughout the gelation step. The as-synthesized alcogels are then dried at ambient pressure by evaporation, eliminating the need for solvent exchange and supercritical drying.

The transformation of a resin to a carbon material requires pyrolysis and activation as a second processing step. Pyrolysis is most often carried out in an inert atmosphere (typically N_2 leading to a carbonization of the polymeric network without significant formation of micropores (pores whose diameter is below 2 nm, as defined by IUPAC [18]). Microporosity is mainly created by an additional activation step, either chemical or physical. Physical activation [3, 19, 20] is often done at more or less the same temperature as the pyrolysis in a mildly oxidizing atmosphere (CO_2). Physical activation is much easier to implement economically than chemical activation and can be applied to a wide range of precursor systems like lignocellulosic materials [21, 22], petroleum coke [1], waste newspaper [23], coconut shell [24] or even waste tires [25]. Here we report a direct, single-step pyrolysis and physical activation protocol for ethanol-based variants of RF organic resins. The chemical identity and microstructural properties of these resins and carbons are analyzed and the impact on

Fig. 1 DSF as applied to the system studied here. S, L and G respectively stand for Solid, Liquid, and Gas. The "/" operator signifies a dispersion of the first system into the second one and the "×" operator signifies an interdispersion of both involved systems

Table 1 Synthesis conditions for materials of the three described different series with varying concentrations of catalyst. EtOH refers to ethanol and HCHO refers to the formaldehyde solutions used in the different series

Series	1st Beaker		2nd Beaker				H_2O: EtOH vol:vol
	Resorcinol [g]	EtOH [mL]	Melamine [g]	HCHO (EtOH) [mL]	HCHO (H_2O) [mL]	EtOH [mL]	
NH**x**-RMF	7.0	15.0	4.0	–	15.0	15.0	0.22 to 0.26
NH**x**-F1.5	7.0	15.0	4.0	–	22.5	7.5	0.43 to 0.49
RF-**x**	7.0	15.0	–	15.0	–	15.0	0.01 to 0.03

the performance of the resulting carbons as water sorbents in heat pumps discussed.

To display this sol–gel process in an intuitive manner, we adhere to the Disperse System Formalism (DSF) [26–28] (Fig. 1). During the reaction, the system goes through the following three states:

Sol state: a dispersion of nanoparticles into a volume-filling liquid phase (i.e., the solvent),
Alcogel state: a co-dispersion of a three-dimensionally percolating solid network within an equally percolating alcohol-based solvent phase,
Dry state: similar to the previous state, except the liquid phase has been replaced by a gas phase (ambient air).

The final step (one-step combined thermal treatment) changes both the chemistry and the microstructure of these materials but not does change the involved states, and is therefore not schematized in this formalism.

2 Materials and methods

2.1 Materials

Paraformaldehyde (Reagent grade, crystalline), formaldehyde (ACS Reagent, 37 wt% aqueous solution stabilized with 10–15 wt% methanol), resorcinol (ReagentPlus 99%), and melamine (99% purity) were all purchased from Sigma-Aldrich and used as-received without further purification. Ammonium hydroxide (ACS Reagent 28.0–30.0% NH_3 basis) was also purchased from Sigma-Aldrich and diluted to 5.5 mol.L^{-1} in deionized water before use. Absolute ethanol (denatured with 5% isopropanol) was used as the primary solvent for the synthesis.

2.2 Synthesis

2.2.1 Synthesis of the resins

A detailed recipe for the different resins described in this work is presented in Table 1. The three variants of RF materials studied in this work are denominated as follows:

RF series: Materials containing resorcinol (R) and formaldehyde (F) but no nitrogen-bearing co-precursor,
RMF series: Samples containing resorcinol and formaldehyde along with melamine (M) as a nitrogen-bearing co-precursor with an F to M molar ratio of 6.3:1,
F1.5 series: Samples based on the above resorcinol, formaldehyde and melamine (RMF) chemistry but with a higher expected degree of crosslinking due to an increased formaldehyde concentration (F to M molar ratio 8:1).

2.2.2 RF series

An ethanolic formaldehyde solution was prepared by dissolving paraformaldehyde in ethanol at 80 °C in a reflux apparatus (round-bottom flask and condenser) for about 2 h, until clarification of the suspension.

Proportions were adjusted so the final concentration of formaldehyde was 37% in mass, as to mimic the weight ratio of the commercial water-based solution. After cooling to room temperature, 100 µL of commercial ammonia were added for each 100 mL of the as-prepared ethanolic formaldehyde solution were added to ensure a total depolymerization of the paraformaldehyde oligomers into monomers. The solution was then kept at 5 °C in the refrigerator to avoid short-term repolymerization.

In a 1st beaker, the resorcinol was dissolved in ethanol and the resulting solution was allowed to stir for 15 min. In a 2nd beaker, the ethanolic formaldehyde solution was preheated to 55 °C. After stirring for 15 min at this temperature, the formaldehyde solution was added dropwise to the 1st beaker and left to stir for another 15 min after the addition had been completed. Gelation was then triggered by the addition of selected amounts of a 5.5 M ammonium hydroxide solution.

2.2.3 RMF and F1.5 series

In a 1st beaker, the resorcinol was dissolved in ethanol and the resulting solution was kept stirring for 15 min. In a 2nd beaker, the commercial formaldehyde solution was heated up to 55 °C and mixed with the melamine until clarification of the sol, at which point the remaining ethanol was added. After a total of 15 min, the resorcinol solution was added dropwise to the MF solution. After 15 min, gelation was triggered by the addition of a 5.5 M ammonium hydroxide solution.

2.2.4 Further processing

As-prepared ammonia-activated sols were then poured in tightly sealed polystyrene molds which had been precovered with a release agent (High Vacuum Grease, Dow Corning) and left to gel and cure at 65 °C for 24 h. The gel bodies were then demolded and resins were allowed to dry over the course of a week in the same oven, releasing porous organic resins.

Regarding sample identification in this publication from now on, RF-x / NHx-RMF / NHx-F1.5 refer respectively to samples of the RF / RMF / F1.5 series with an added amount of ammonium hydroxide such as its final concentration in the sol before gelation is x mmol.L^{-1}.

2.3 Pyrolysis and activation

Pyrolysis and physical activation were carried out as a single step inside a tube furnace (Borel TU 1200-105-900). For this purpose, resins were placed in a quartz boat inside the furnace, which was purged with CO_2 (Messer 3.0, 99.9% purity) for 20 min prior to heating up the furnace to 800 °C at a rate of 5 °C.min^{-1} with a constant CO_2 flow of 0.7 L.min^{-1}. After a holding time of 4 h, the furnace was then cooled down to room temperature over the course of 10 h.

2.4 Characterization

Elemental analysis (C, H, N) was carried out on a LECO TruSpec Micro, after thoroughly drying the samples overnight in nitrogen sorption tubes at 200 °C and 1.3×10^{-2} mbar. The C and H contents were determined by infrared spectroscopy and the N content by thermal conductivity measurements of the gas phase. The O content was deduced from the remaining unattributed mass, thus assuming the absence of quantitative inorganic impurities. Measurements were carried once with an accuracy of ±0.3%.

X-ray diffraction was realized on a PANanalytical X'Pert PRO apparatus with a Bragg-Brentano geometry, using $Cu_{K\alpha}$ monochromatic light ($\lambda = 1.5406$ Å). The average size of nanocrystalline domains was calculated using Scherrer's equation (with the shape factor set as $K = 0.9$) and the spacing between graphitic planes within these domains was estimated using Bragg's equation. Intensities have then been normalized with regard to the signal maximum in the $\theta = 10°$ to $\theta = 60°$ range. Multiple measurements were carried out for improved statistics and the calculated standard deviation is reported.

Envelope density measurements were carried out on a powder displacement device (GeoPyc 1360, micromeritics) with a consolidation force of 4.0 N and a conversion factor of 0.1246 $cm^3.mm^{-1}$. Ten consecutive measurements were realized on each sample and the average value was retained. Measurements were repeated on three fragments of each material, each of them undergoing 10 cycles, for a total of 30 measurements. Since the intrinsic error on the measurement is small for the type of materials under investigation, the variation reported in this case is the calculated standard deviation.

Skeletal density was measured *via* helium pycnometry (AccuPyc II 1340, micromeritics) using 134.447 kPa as both purging and measuring pressures. Thirty purges followed by thirty measuring cycles were realized on each sample and the average value was retained. Per material, one such measurement cycle was carried out and the corresponding standard deviation reported.

Nitrogen and carbon dioxide sorption isotherms were recorded at respectively 77 K and 273 K (3Flex, micromeritics). Prior to each measurement, samples were degassed at 200 °C for 1200 min at a pressure of 1.3×10^{-2} mbar. In situ degassing was also executed directly within the sorption apparatus before each carbon dioxide sorption measurement at a pressure of 6.7×10^{-2} mbar. Micropore and mesopore volumes as well as micropore surface areas were measured using state-of-the-art nitrogen physisorption NLDFT kernels (according to the ISO-15901-3 standard [29]). CO_2 physisorption and its corresponding NLDFT kernel was also used to characterize activated carbons to quantify the expected ultramicroporosity formed primarily during the physical activation process, which cannot reasonably be assessed by nitrogen physisorption at 77 K because of the very low diffusivity of the N_2 sorbate at this temperature. Results were analyzed using combined CO_2

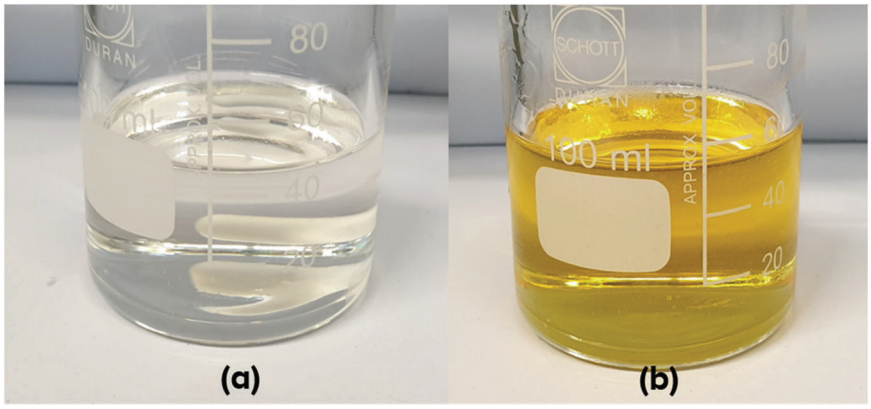

Fig. 2 Visual appearance of an RMF sol before (**a**) and after (**b**) addition of catalytic ammonium hydroxide

and N_2 sorption isotherms *via* NLDFT kernels integrated in the micromeritics software. A graphitic slit geometry was assumed for micropores while a cylindrical geometry was assumed for mesopores, based on Olivier's [30, 31] and Tarazona's [32, 33] works.

Scanning electron microscopy (Nova NanoSEM 230 FEI) was used to acquire micrographs of the carbonaceous samples using a Through-Lens Detector (TLD) with a working distance of 4 mm under an accelerating voltage of 5.0 kV. Samples were freshly cleaved and observed without any coating or sputtering. Selected micrographs were further subjected to image analysis to determine particle size distributions.

Thermal conductivity was measured for $32 \times 32 \times 8\ mm^3$ monolithic samples on a homemade guarded hot place device described elsewhere [34] at 30 °C and 50% relative humidity (room conditions). Measurements were carried once with an absolute error in the range of $\pm 2\ mW.m^{-1}.K^{-1}$ on samples with such geometry and dimensions, which should be added to the relative error arising from experimental deviations on triplicates.

Dynamic vapor sorption isotherms were recorded on an isothermal gravimetric device (VTI-SA + Water Vapor Sorption Analyzer, Porotec) at 50 °C with relative humidities (RH) ranging from 0% to 75%. Measurements were carried out on granulated samples previously dried in situ at 90 °C under a nitrogen atmosphere. Equilibrium conditions for each step were set for a mass change of less than 0.02% over 10 min.

3 Results and discussion

When adapting a given recipe to a different chemistry (or solvent system) by changing a parameter, it is not always possible to keep all other parameters constant. In this work, we opted to keep the total reaction volume (before addition of the catalyst) as well as the initial resorcinol concentration constant for all preparations. The dilution ratio ((Water + Ethanol + Methanol)/(R + M + F) $\in \{3.2, 4.3\}$ mol/mol) was kept almost constant within a series (Table 1) and the water-to-ethanol volumetric ratio (H_2O/EtOH $\in \{0.01, 0.49\}$ vol/vol) changed only slightly between different series but was virtually constant within one.

For all three series, upon catalyst addition the sols quickly turned to a bright, sunflower yellow color while retaining translucence (Fig. 2). The color intensity increased with the amount of catalyst added. After being put in a 65 °C oven, sols quickly became opaque, reaching different shades of brown, from very light (low catalyst amount) to quite dark (high catalyst amount). This shift in optical properties, faster for larger catalyst amounts, is a witness of polycondensation reactions, nanoparticle nucleation and eventually solid network formation. Gelation typically took a few hours in the 65 °C curing oven, at which point the gel bodies were still rather soft (depending on catalyst concentration), but could be handled safely generally after 1 day. Resin-gels were left inside the curing oven for about 1 week, causing them to dry by evaporation of the pore fluid, eventually leaving behind the resin green bodies.

Based on these observations, monoliths discussed here differ from Pekala's transparent dark-red aerogels. Samples with a Pekala-like appearance could be obtained by drastically reducing the catalyst concentration in the sol down to a value of around $4\ mmol.L^{-1}$, in which case gelation happened slowly over a period of almost a week at 65 °C, another week being necessary for the drying process. However, these materials are not included in this study because due to their higher initial envelope density they did not remain monolithic after pyrolysis and activation. However, our goal was to obtain monolithic activated carbons with a hierarchical pore structure featuring a close to optimal compromise between heat and mass transfer. Higher sol concentrations of ammonium hydroxide, up to around $1\ mol.L^{-1}$, were also investigated. The resulting materials, while remaining monolithic upon gelation and curing, led to extremely dusty and mechanically unstable carbons after pyrolysis/activation which is why they were

Table 2 Elemental analysis conducted on resins and corresponding activated carbons

Sample	C at.% ±0.3%	H at.% ±0.3%	N at.% ±0.3%	O at.% ±0.3%	O/C at.	N/C at.	N/C at. In the sol
Resins							
NH64-RMF	37.2%	43.6%	8.7%	10.5%	0.28	0.23	0.28
NH160-RMF	35.2%	43.7%	9.5%	11.6%	0.33	0.27	0.28
NH256-RMF	37.1%	42.2%	9.3%	11.3%	0.30	0.25	0.28
NH64-F1.5	35.4%	44.3%	8.8%	11.6%	0.33	0.25	0.24
NH160-F1.5	34.6%	44.3%	8.7%	12.4%	0.36	0.25	0.24
NH256-F1.5	34.3%	44.1%	8.8%	12.7%	0.37	0.26	0.24
Carbons							
NH64-RMF	69.6%	18.4%	3.4%	8.7%	0.12	0.05	–
NH160-RMF	66.5%	20.1%	2.9%	10.5%	0.16	0.04	–
NH256-RMF	66.1%	20.9%	2.7%	10.3%	0.16	0.04	–
NH64-F1.5	73.5%	16.1%	4.1%	6.3%	0.09	0.06	–
NH160-F1.5	74.6%	16.4%	4.1%	4.8%	0.07	0.06	–
NH256-F1.5	72.4%	16.8%	4.2%	6.6%	0.09	0.06	–
RF-64	78.6%	14.9%	–	6.4%	0.08	–	–
RF-160	79.4%	13.4%	–	7.2%	0.09	–	–
RF-256	78.2%	13.5%	–	8.3%	0.11	–	–

also excluded from this study, while here we focus on materials prepared from ammonia concentrations ranging from 64 to 256 mmol.L^{-1}.

The dissolution of resorcinol, which has been chosen for its rapid condensation kinetics with formaldehyde [35], quickly leads to the formation of nanometric colloidal building blocks with different degrees of hydroxymethylation. Paraformaldehyde cracking into formaldehyde monomers is a technique commonly used in histology to circumvent the issues of commercial formaldehyde (acidity, possible partial repolymerization despite the methanol content, impurity, …) and has been transposed here (in the RF series) to obtain an ethanolic 37% (in mass) formaldehyde solution. Of note, a completely anhydrous state could be reached by changing the catalyst, as the ammonium hydroxide used herein is water-based. The last column of Table 1 recaps the water-to-ethanol volumetric ratio in the three considered series.

Nitrogen-doping with melamine was however found to be more difficult to realize in a completely water-free system, because of the very low solubility of melamine in pure ethanol. Separate tests showed that an amount of water equivalent to the one contained in commercial formaldehyde solutions coincided with the minimal water concentration needed for the melamine to dissolve. Therefore commercial formaldehyde solutions were used for the RMF and F1.5 synthesis, despite considerably modifying the water to ethanol ratio; however, the reaction volume before catalyst addition was kept constant.

The dissolution of melamine, or rather its condensation with formaldehyde into hydroxymethylated moieties [36], is known to be sensitive to different factors such as pH, relative concentrations, and temperature [37, 38]. It has also been shown in the literature that increasing the availability of hydroxymethyl derivatives increases the solubility of melamine [39]. From here, the most prevalent issue with the N-doping of the RF system is that melamine is usually only weakly incorporated within the backbone of the material because of its low degree of condensation with formaldehyde at the originally chosen molar ratio. This leads to most of N-bearing dopants being lost during pyrolysis and activation. Therefore, a way to increase the final amount of nitrogen contained within the material, explored in this study, is to increase the initial quantity of formaldehyde rather than the melamine concentration [40, 41]. The F:M molar ratio was thus varied from 6.3 (RMF series) to 8 (F1.5 series) in an attempt to increase the crosslinking density and hence the covalent bonding character of these species. At the origin of this hypothesis stands a statistically complete condensation of formaldehyde on all available sites for each melamine molecule, effectively resulting in complete conversion to a hexa-hydroxymethylated state, which should allow this modified melamine precursor to react more readily with itself and with the resorcinol polycondensate network.

3.1 Chemical composition and molecular structure

The atomic compositions from elemental analysis (Table 2) are in the expected range for this kind of materials [13]. Due to a larger amount of formaldehyde in the F1.5 series recipe, melamine and resorcinol moieties are expected to

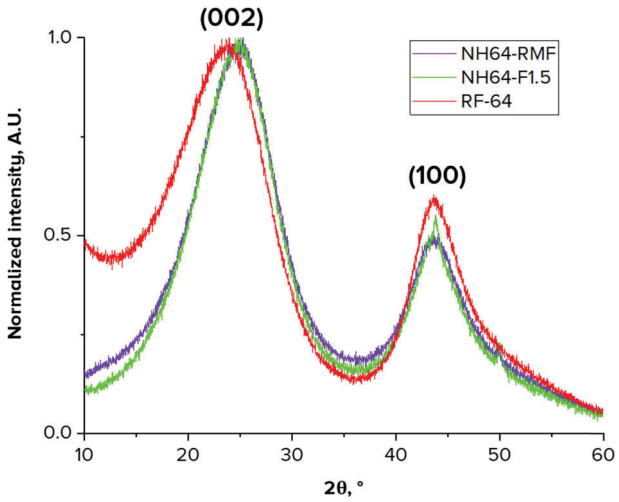

Fig. 3 X-ray diffractograms of an activated carbon from each of the RMF, F1.5, and RF series. Intensities have been normalized in respect to the (002) peak and angles have been narrowed to relevant angles within the 10–60° range

statistically undergo hydroxymethylation on more of their available sites. Therefore, the higher amount of oxygen in the F1.5 resins compared to the RMF resins is a good indicator of a higher hydroxymethylation degree of the melamine. Another consequence of this is a decrease in the nitrogen content in the F1.5 series when expressed percentwise. This is due to a larger amount of C, H, and O in the F1.5 resins resulting from more formaldehyde being substituted onto aromatic moieties. As illustrated by the N/C ratio in the sols (last column of Table 2), melamine molecules are well incorporated within the solid backbone of the materials from both RMF and F1.5 series. However, when comparing the N/C content in the sol, the ratio increases during gelation for the F1.5 series and decreases for the RMF series. In addition, after pyrolysis the nitrogen content is higher in the F1.5 series than in the RMF series, which is a strong indication of the better integration of melamine in the F1.5 series. In fact previously reported XPS results of melamine and urea containing resins show that the originally pyridinic nitrogen gets partially converted to quaternary nitrogen and to a lesser extent to pyridine nitrogen oxide as well as probably pyrrolic or pyridine type nitrogen upon pyrolysis [13, 42, 43]. The oxygen content is also significantly lower in F1.5 carbons, possibly pointing towards a large amount of non-crosslinked hydroxymethylated formaldehyde moieties that were removed during the thermal treatment.

It is therefore not surprising that the carbon elemental content in the activated carbons of the F1.5 series is higher than in their RMF counterparts. In fact, it is interesting to note that the F1.5 series is much closer to the RF series in terms of oxygen to carbon ratio than the RMF series, although—as we have targeted in the experimental planning—it contains more nitrogen (see Table 2). Contrary to the RMF activated carbons (Table 2) for which the addition of melamine leads to an increase of not only the nitrogen, but also the oxygen and hydrogen contents, in the F1.5 series only the hydrogen content increases to some extent, but significantly less than for the RMF series. This can be seen as an indication that the nitrogen in the F1.5 series is indeed more directly incorporated in the graphitic crystallites of the carbon structure resin/carbon structure rather than as side groups.

Successful carbonization during the heat treatment can be observed through the increased carbon content (Table 2) and graphite peaks observable by X-ray diffraction (Fig. 3). The normalized diffractograms of carbons from the three different series appear almost identical, strongly indicating a similar polycyclic aromatic substructure and packing (Fig. 3), the biggest difference being the larger low-angle background signal for the RF series. This similarity connecting the different series is also confirmed by the crystallite sizes in both (002) and (100) directions calculated according to Scherrer's equation [44] as well as the observed d_{002}-spacing (Table 3). This means that the presence of nitrogen-bearing precursors at 3-4 atomic percent, independently of how it is incorporated (RMF and F1.5 series), does not seem to have an observable influence on the carbonaceous phase domain sizes.

The calculated crystallite size is similar to the values previously reported by Huber et al. [13] (A-p900-CO2-3h) for water-based RMF materials pyrolyzed and physically activated in two separate steps.

3.2 Microstructure assessment

The variation of skeletal density values for both resins and carbons within a series was found to lie within the measurement error range. Resins of the RMF, F1.5, and RF series have a skeletal density of respectively 1.33, 1.29, and 1.31 ± 0.02 g.cm^{-3}. The activated carbons of these series have a skeletal density of respectively 1.91, 1.64, and 1.80 ± 0.03 g.cm^{-3}. These values are in the expected range according to previous in-house work on similar materials [13] and elemental composition (Table 2). An exception are the carbons from the F1.5 series, which despite the higher carbon content compared to the RMF series, have a remarkably low skeletal density. Possible explanations could be sought either in a difference in oxygen chemical bonding states, surface chemistry, polycyclic aromatic domain packing or topological effects hindering the penetration of helium [45].

Contrary to the skeletal density, the envelope density of resins (Fig. 4, left) and carbons (Fig. 4, right) generally follows a decreasing trend with an increasing amount of ammonium hydroxide catalyst. Combined with the constant

Table 3 Calculated crystalline domain sizes and average spacing between graphitic planes of carbon samples from the RMF, F1.5, RF series, as well as a comparable sample from Huber et al. [13]

Sample	Scherrer's size, Å (002)	Scherrer's size, Å (100)	Bragg's distance (002)
NH64-RMF	9.5	15	3.6
NH160-RMF	9.0 ± 0.6	13.2 ± 0.9	3.6 ± 0.1
NH256-RMF	9.1 ± 0.2	14.2 ± 2.2	3.6 ± 0.1
NH64-F1.5	9.3 ± 0.2	14.7 ± 2.1	3.6 ± 0.1
NH160-F1.5	9.1 ± 0.2	13.9 ± 1.3	3.6 ± 0.1
NH256-F1.5	9.1 ± 0.2	12.8 ± 0.3	3.7 ± 0.1
RF-64	9.2	14.1	3.7
RF-160	9.2 ± 0.1	14.4 ± 0.2	3.7 ± 0.1
RF-256	9.2 ± 0.1	14.0 ± 1.1	3.7 ± 0.1
A-p900-CO2-3h*	8	17	3.7

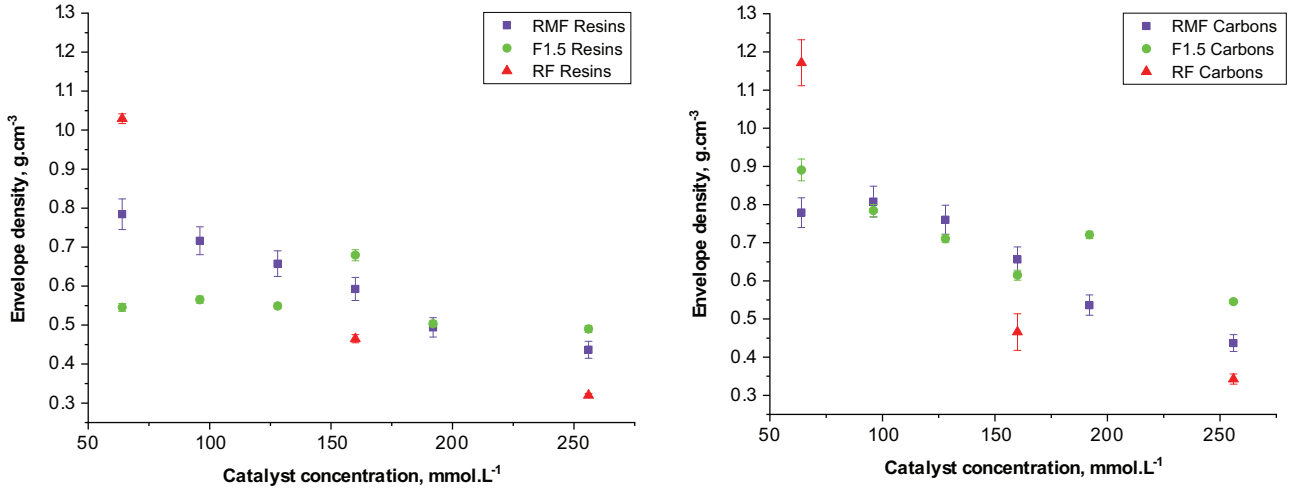

Fig. 4 Envelope density measurements of resins and carbons from the RMF, F1.5, and RF series. Purple squares represent samples from the RMF series, green discs represent samples from the F1.5 series, and red triangles represent samples from the RF series

Table 4 Impact of the heat treatment on the mass and volume of samples from the RMF, F1.5, and RF series

Sample series	Volumetric shrinkage	Mass loss
NHx-RMF	65.2 ± 0.9%	62.5 ± 1.7%
NHx-F1.5	73.4 ± 5.1%	66.7 ± 0.7%
RF-x	55.4 ± 2.3%	52.4 ± 0.1%

skeletal density within a series, the decreasing envelope density indicates an increase of the total pore volume with increasing catalyst concentration. An exception to this observation is the envelope density of the F1.5 resins before pyrolysis, where no clear trend can be observed. Instead, the envelope density before pyrolysis is almost constant with changing catalyst concentration, with a discontinuity at a catalyst concentration of ~160 mmol.L^{-1}. This discontinuity is to some extent still observable after pyrolysis, where the generally decreasing envelope density suddenly increases between 160 and 200 mmol.L^{-1} before decreasing again. This is not an outlier, as the same recipe + catalyst range has been probed multiple times with the same outcome.

During pyrolysis and activation, resins undergo mass loss as well as isotropic shrinkage. Because the relative importance of the two phenomena varies from material to material, the resulting activated carbons can be denser or lighter than their corresponding resins. The average values of shrinkage and mass loss for the different series are shown in Table 4. Although mass loss during pyrolysis seems consistent within a series - that is for a given "chemistry" -, volumetric shrinkage tends to vary more between compositions, causing more variability in the overall densification process. As expected due to the loss of the majority of the nitrogen-bearing moieties during pyrolysis, the mass loss is higher for the nitrogen-containing series RMF and F1.5. Interestingly enough, the mass loss is higher in the F1.5 series than in the RMF series despite the smaller changes in the nitrogen to carbon (N/C) ratio during pyrolysis. The F1.5 series also stands out with respect to

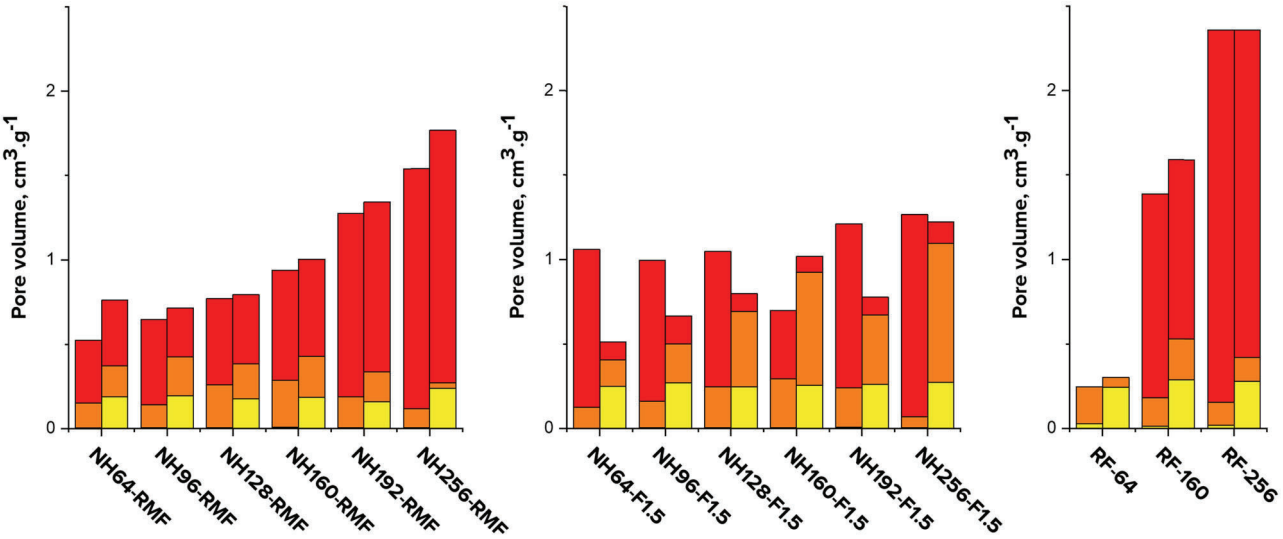

Fig. 5 Porosity repartition of resins and activated carbons of the RMF, F1.5, and RF series: for each duo of stacked columns, the resin is on the left and the carbon is on the right. The yellow part (bottom) represents the microporosity, the orange part (middle) represents the mesoporosity, and the red part (top) represents the macroporosity

densification during pyrolysis. For the RF and RMF series, shrinkage and mass loss almost compensate each other, leading to equal or only slightly higher densities after pyrolysis (see Fig. 4). On the other hand, for the F1.5 series, the shrinkage is significantly higher than the mass loss, leading to a significant overall densification. This is not understood in detail at the moment, but the implied message is that despite the higher formaldehyde content in the mixture the overall degree of crosslinking in the resin seems lower when all species including resorcinol are considered. Another possible explanation is that the microstructural topology is affected by the (surface) chemistry in such a way as to favor pore collapse. One must also note that this effect is only really prominent at lower catalyst concentrations. Again, an exception within the series is the F1.5 sample with a catalyst concentration of 160 mmol.L^{-1}, whose density decreases during pyrolysis.

We do not report BET surface areas in the main text of this study, despite this value being a popular benchmark measurement in the literature for porous materials. Indeed, even with the modified equation proposed by Llewelyn et al. [46] and using lower than usual relative pressures (between 5.10^{-3} and 0.03), the classical BET model remains intrinsically unadapted for the materials studied here which contain both meso- and micropores [47] (For comparison with other work, values for BET surface areas can be found in Table S2) Instead, we discuss the pore volumes in different size ranges. The total pore volume $\left(V_{pore} = \frac{1}{\rho_{envelope}} - \frac{1}{\rho_{skeletal}}\right)$ of resins and carbons was calculated using their envelope density $(\rho_{envelope})$ and their skeletal density$(\rho_{skeletal})$. The micro- and mesopore volumes were estimated based on the NLDFT interpretation of N_2 and CO_2 sorption isotherms (see materials and methods). The remaining part of the total pore volume is considered to represent the material's macroporosity.

The resins before pyrolysis do not contain any or negligible amounts of microporosity (Fig. 5). The meso- and macroporosity of the resins on the other hand show a clear dependence on the catalyst concentration. This also leads to low surface areas as estimated by NLDFT in the order of 759 ± 85 m^2.g^{-1} for the RMF series, 959 ± 41 m^2.g^{-1} for the F1.5 series, and 954 ± 56 m^2.g^{-1} for the RF series (see supplementary informations for further details). The observed dependence however is reliant on the considered series and thus on the exact chemistry of the system. In the melamine containing RMF and F1.5 series, the mesoporosity of the resins reaches a maximum at a catalyst concentration of 160 mmol.L^{-1}. In contrast, in the RF series the amount of mesoporosity decreases with an increasing catalyst concentration. The amount of macroporosity increases continuously with an increasing catalyst concentration for the RMF and RF series. For the F1.5 series however, the amount of macroporosity reaches a minimum at a catalyst concentration of 160 mmol.L^{-1}. Comparing our results to those of Rey-Raap et al. [48], where they observed inverse trends for the meso- and macroporosity for RF resins in classical aqueous systems, we do observe this for the F1.5 and RF series in our ethanol-based counterparts, but not for the RMF series, where at small catalyst concentrations both the meso- and macroporosity seem to increase.

Comparing the pyrolyzed carbon samples to the resins (Fig. 5), one can clearly observe the creation of significant microporosity in the carbon materials during the combined

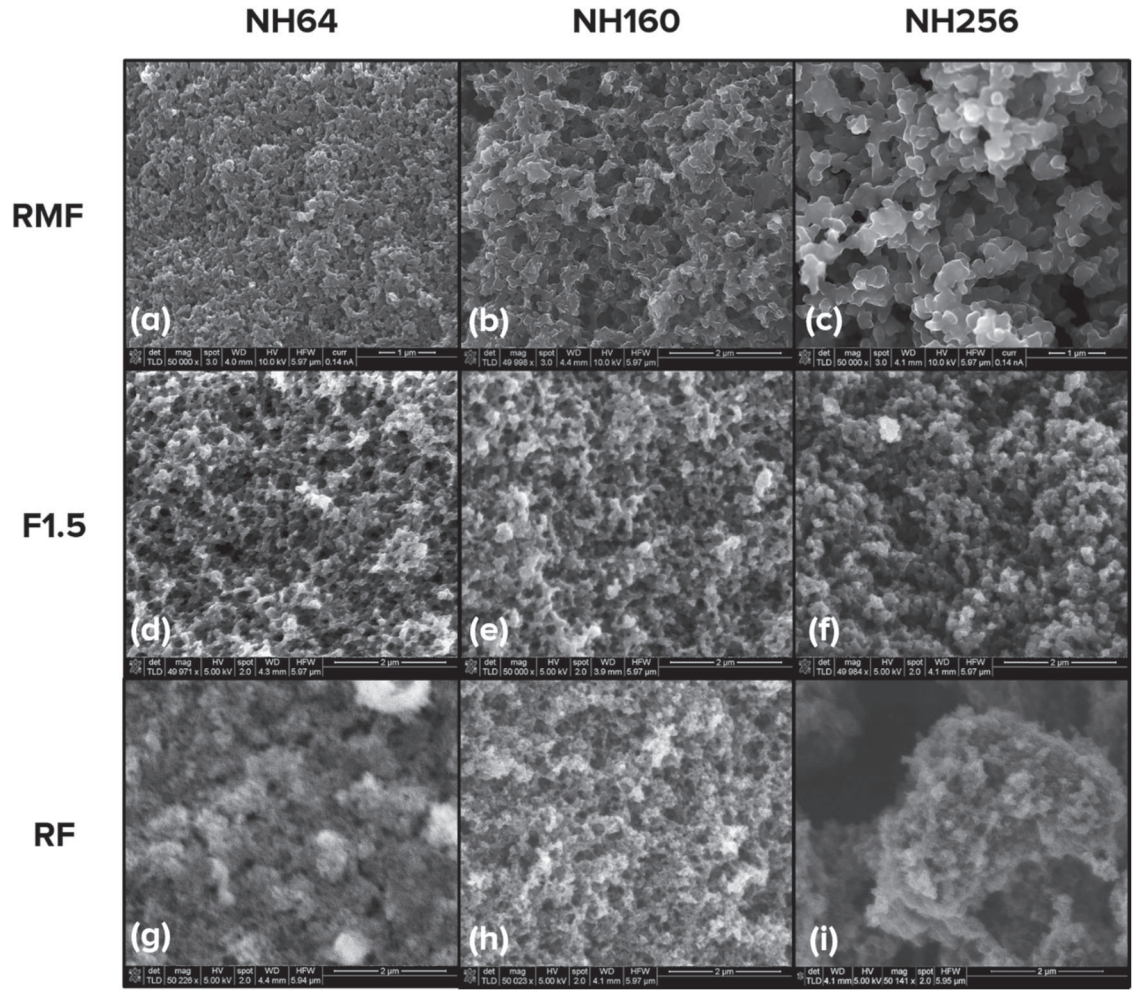

Fig. 6 SEM micrographs of carbon samples from all three series studied here. Top row: NH64-RMF (**a**), NH160-RMF (**b**), and NH256-RMF (**c**). Middle row: NH64-F1.5 (**d**), NH160-F1.5 (**e**), and NH256-F1.5 (**f**). Bottom row: RF-64 (**g**), RF-160 (**h**), and RF-256 (**i**)

pyrolysis/activation step; activation is primarily responsible for micropore formation. The creation of microporosity is qualitatively also visible when observing the sorption isotherms (Figs. S5–S7 of the supplementary materials). Within one series the amount of microporosity varies very little (Fig. 5; it reaches consequent values of around 0.20 $cm^3.g^{-1}$ for the RMF carbons, and 0.25 $cm^3.g^{-1}$ for the F1.5 and RF carbons.) This indicates little dependence on the starting microstructure of the resins but the extent depends largely on the physical CO_2 activation protocol. Therefore, tailoring the microporosity of these materials should be possible by means of process parameters adjustment.

In contrast to this, the meso- and macroporosity seem to be mainly dependent on the starting microstructure of the resins. For the RMF and RF series, the relative proportions or meso- and macroporosity is very similar before and after pyrolysis, with the volume of each category remaining similar or decreasing slightly. However, due to the created microporosity, the total pore volume has a tendency to increase slightly within these two series, explaining the larger changes in skeletal than envelope density observed above (Fig. 4 and Table 4). However, in the F1.5 series, there is a sharp decrease in the amount of macroporosity that is concomitant with a very substantial increase in the amount of mesoporosity, while some microporosity is also created. Even though this is certainly linked in part to the densification of the material discussed above, it remains a very intriguing finding. It is also commensurate with the finer overall microstructure of the F1.5 series presented below.

For water-based recipes, Rey-Raap et al. have hypothesized that observed changes in the microstructure of the resins have different origins: promotion of primary particle growth by the catalyst, and a further dilution of the system that increases the space between particles which leads to an increase in both pore size and total pore volume, until a maximum possible dilution is reached. Past this dilution

Table 5 Thermal conductivity (λ, unit is $mW.m^{-1}.K^{-1}$) of carbons from the RMF, F1.5, and RF series

Sample	λ	Sample	λ	Sample	λ
NH64-RMF	135.6 ± 8.4	NH64-F1.5	104.9 ± 5.4	RF-64	154.4 ± 1.5
NH160-RMF	97.1 ± 3.3	NH160-F1.5	113.9 ± 4.2	RF-160	113.9 ± 4.1
NH256-RMF	98.6 ± 0.6	NH256-F1.5	120 ± 0.9	RF-256	76.1 ± 1.3

threshold, the larger pores start collapsing and the macropore volume decreases again. Rey-Raap et al. further proposed that the dilution corresponding to this inflection point depends on the mechanical strength of the solid skeleton and thus on the primary particle size and the pH [48]. The confirmation of these effects by SEM is difficult due to two reasons: it is not possible to polish the highly porous resins, instead uneven fracture surfaces have to be observed which are much more difficult to interpret. The resins are also non-conductive and have to be sputtered to be observed by SEM. However, the sputtering of these uneven porous surfaces is likely to influence the observed microstructures. A way around this is to look at the microstructure of the carbon samples after pyrolysis [49]. SEM micrographs of our ethanol-based carbon samples for the different series can be found in Fig. 6. Despite the observed changes in meso- and macroporosity by varying the catalyst concentration (Fig. 5), only the RMF series shows a similar evolution of the primary particle size as reported in literature for water-based resorcinol–formaldehyde resins/carbons [48–51]. This was further corroborated by means of image analysis to determine the characteristic size of microstructural features in a more quantitative manner (see supplementary materials). The observed structural differences are most likely linked to the structure formation step and the chemistry in particular. First off, the ethanol-based solvent system completely changes the solubility of the monomers but more importantly of the growing polycondensates in the pre-primary particle forming stage. The water/ethanol ratio in this work was varied between 0.01 and 0.49. Changes in the dilution ratio are however on a smaller scale in our study than in the work of Rey-Raap et al. and are thus less prone to induce major microstructural changes. Although a pH value is difficult to define in these conditions, the effect of the catalyst concentration should not be affected much in mechanistic terms. One thing to consider is also that the variation in catalyst concentration has a secondary effect on the alcohol solvent system's overall polarity, altering at least partially the ionic strength in the solvent phase thus affecting the interparticle potential in the colloidal system and thus the agglomeration and gelation process dynamics. An indication for this can be seen with the microstructure observed for the RF system at the highest catalyst concentration (Fig. 6i), which looks to be the result of a two-step agglomeration process, where percolation happens through the agglomeration of secondary particles, leading to large scale porosity between secondary particles and mesoporosity between the primary particles within the secondary particles.

The thermal conductivity of activated carbons was measured on monolithic samples and the results are summarized in Table 5. Thermal conductivity is an important property for some applications (e.g., adsorption heat pumps), where the material is cycled between two temperature levels and a good thermal diffusivity α (which will also result in a high thermal conductivity $\lambda = \alpha\rho C_p$, where C_p is the specific heat capacity) leads to faster cycle times. Two phenomena can be expected to dominate the evolution of thermal conductivity between these activated carbons. Firstly, the partial graphitization that arises during the heat treatment can be expected to lead to a higher thermal conductivity of the solid backbone. Secondly, a high amount of meso- and microporosity is known to significantly decrease the thermal conductivity of a material.

From this starting point, the measured values are indeed in the expected range [13] (with a large spread from 76 to 154 $mW.m^{-1}K^{-1}$). Based on previous measurements, materials with chemical composition, atomic structure, porosity and thermal conductivity in the range observed here show fast adsorption/desorption cycles interesting for adsorption heat pump applications [13]. The measured conductivities mostly follow the expected trend of higher porosities (see Fig. 4) leading to lower conductivities. The similar measured thermal conductivity for NH160-RMF and NH256-RMF can be explained by the larger amount of mesoporosity in the former, which has a more drastic effect on the thermal conductivity than macroporosity [52]. Smaller variations in the values can be explained by more subtle changes in the microstructure (e.g., size and morphology of the macroporosity) as well as changes of the atomic/nanoscale structure. For instance, the observed trend in thermal conductivity could come from crystallinity differences, from a quantitative point of view. The XRD analysis proposed herein only offers qualitative insights and cannot significantly discriminate between the RMF, F1.5, and RF series (Table 3): it is not very sensitive to the total amount of larger polyaromatic graphitized domains compared to amorphous ones within the solid backbone of materials, or even their interconnectivity. More realistically, the observed differences and trends in thermal conductivity for these carbons probably arise primarily from microstructural differences and the related change in solid network conductivity, which is also in good qualitative agreement with SEM images.

The water uptake of carbon samples was characterized by recording their mass change following equilibration at

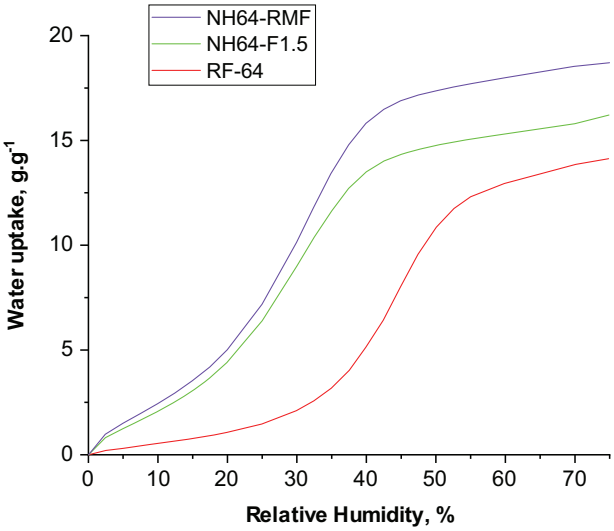

Fig. 7 Adsorption branches of dynamic vapor sorption isotherms from one carbon sample of each of the RMF, F1.5, and RF series; all synthesized with the same amount of catalyst

different relative humidities ranging from 0% to 75% (Fig. 7) using a dynamic vapor sorption (DVS) apparatus. One carbon from each series was chosen, and all three of them had the same initial catalyst concentration to allow for a ready comparison. The current measurements serve as a quick benchmark test for the water sorption potential of these materials. Further investigations including reproducibility, kinetics of adsorption, and hysteresis behavior would be needed to optimize these materials towards a specific application. Such extended sorption studies on these materials will be the focus of a follow-up publication.

DVS isotherms for the RMF and F1.5 carbons are very similar. For the carbons studied in this work, the relative differences can be sought in either a difference in surface chemistry or pore structure. The activated carbon from the F1.5 series for example contains significantly less oxygen but more nitrogen than its RMF counterpart (see Table 2). The activated carbon from the RF series displays a lower total sorption although its adsorption curve is also S-shaped. Its lower water uptake capacity is readily explained by a lower amount of micro- and mesoporosity. Also, the RF activated carbon adsorbs water at higher relative humidities than its N-bearing RMF and F1.5 counterparts do, which is in good agreement with the literature [53]. However, despite having the highest nitrogen content, the carbon from the F1.5 series displays a behavior similar to the RMF carbon and its isotherm is not shifted further towards earlier adsorption, which comes as somewhat of a surprise. The lower oxygen content in the F1.5 series and more generally the difference in surface chemistry and topology is most likely responsible for the observed behavior.

4 Conclusions

In this work, we demonstrated the transposability of a porous phenolic resin recipe from an aqueous to an ethanol-based solvent system for three selected chemistries. This adapted recipe is now compatible with inorganic alcohol-based chemistries such as a classical two-step, TEOS based, silica sol–gel process, bringing it in the direct scope of our future investigations—the elaboration of hybrid organic-inorganic systems. As a pleasant side effect, the change of solvent system also removes tedious preliminary solvent exchange steps that are usually necessary for supercritical state drying processes.

The monolithic activated carbons prepared in this study, as well as their properties were strongly influenced by all three studied chemical synthesis parameters, namely (i) the change in the solvent system, (ii) the catalyst concentration and (iii) the amount of formaldehyde (RMF only). Interestingly, the influence of the catalyst concentration on the microstructure runs exactly contrary to observations from the literature for water-based phenolic resins. Note also, that the synthesis protocols still employed some amount of water in the solvent system, particularly in the RMF system where water was necessary to allow dissolution of the melamine precursor.

Melamine containing RMF resins were able to retain considerable amounts of nitrogen (3–4%, atomic percentage) upon pyrolysis, particularly for the F1.5 system with more formaldehyde and without increasing the initial amount of nitrogen-containing co-precursor. These variations in the starting chemistry led to unexpectedly dissimilar materials with significant property differences (porosity, microstructure, thermal conductivity). In addition, the microstructure of the F1.5 system seems pretty much unaffected by the catalyst concentration which is a first observation of its kind in this class of materials.

Although the meso- and macroporosities can be tailored to some extent through synthesis parameters, it seems that regardless of the variation on the specific resin chemistry, it is mainly the activation treatment that creates microporosity.

In conclusion, we were able to synthesize monolithic, porous, and mostly amorphous activated carbons with nanocrystalline domains using an alcohol-based phenolic resin chemistry. These carbons displayed a relatively high thermal conductivity as well as good water sorption properties, thus making them an interesting class of materials as sorbents in heat pumps and waste-heat related applications. More importantly, the protocol described here opens up new avenues for the preparation of hybrid inorganic/organic composite materials by a straightforward combination with classical two-step acid-base catalyzed alkoxysilane sol–gel

chemistry and their corresponding oxide/carbon or oxycarbide analogues.

Acknowledgements The authors would like to thank the Laboratory for Organic Chemistry at ETH Zürich for the elemental analysis, Dr Arndt Remhof at Empa for allowing us to use his X-ray diffractometer, and the Cellulose & Wood Materials laboratory at Empa for the measuring time on their DVS apparatus.

Funding MMK gratefully acknowledges financial support from the Swiss National Science Foundation (Grant number IZLRZ2_164058).

Compliance with ethical standards

Conflict of interest The authors declare that they have no conflict of interest.

References

1. Kubota M, Ito T, Watanabe F, Matsuda H (2011) Pore structure and water adsorptivity of petroleum coke-derived activated carbon for adsorption heat pump–Influence of hydrogen content of coke. Appl Therm Eng 31(8–9):1495–1498. https://doi.org/10.1016/j.applthermaleng.2011.01.036
2. Shimooka S et al. (2007) Improvement of water adsorptivity of activated carbon for adsorption heat pump by hydrophilic treatment. Proc Int Symp EcoTopia Sci
3. Kawano T, Kubota M, Onyango MS, Watanabe F, Matsuda H (2008) Preparation of activated carbon from petroleum coke by KOH chemical activation for adsorption heat pump. Appl Therm Eng 28(8–9):865–871. https://doi.org/10.1016/j.applthermaleng.2007.07.009
4. Pekala RW (1989) Organic aerogels from the polycondensation of resorcinol with formaldehyde. J Mater Sci 24(9):3221–3227
5. Wang H, Bo X, Zhang Y, Guo L (2013) Sulfur-doped ordered mesoporous carbon with high electrocatalytic activity for oxygen reduction. Electrochim Acta 108:404–411. https://doi.org/10.1016/j.electacta.2013.06.133
6. Paraknowitsch JP, Thomas A (2013) Doping carbons beyond nitrogen: an overview of advanced heteroatom doped carbons with boron, sulphur and phosphorus for energy applications. Energy Environ Sci 6(10):2839. https://doi.org/10.1039/c3ee41444b
7. Lermontov SA et al. (2017) Facile synthesis of fluorinated resorcinol-formaldehyde aerogels. J Fluor Chem 193:1–7. https://doi.org/10.1016/j.jfluchem.2016.11.001
8. Ding S, Zheng S, Xie M, Peng L, Guo X, Ding W (2011) One-pot synthesis of boron-doped mesoporous carbon with boric acid as a multifunction reagent. Microporous Mesoporous Mater 142 (2–3):609–613. https://doi.org/10.1016/j.micromeso.2011.01.003
9. Rao CNR, Gopalakrishnan K, Govindaraj A (2014) Synthesis, properties and applications of graphene doped with boron, nitrogen and other elements. Nano Today 9(3):324–343. https://doi.org/10.1016/j.nantod.2014.04.010
10. Liu X et al. (2014) From melamine–resorcinol–formaldehyde to nitrogen-doped carbon xerogels with micro- and meso-pores for lithium batteries. J Mater Chem A 2(35):14429–14438. https://doi.org/10.1039/C4TA02928C
11. Principe IA, Fletcher AJ (2018) Parametric study of factors affecting melamine-resorcinol-formaldehyde xerogels properties. Mater Today Chem 7:5–14. https://doi.org/10.1016/j.mtchem.2017.11.002
12. Salinas-Torres D, Léonard AF, Stergiopoulos V, Busby Y, Pireaux J-J, Job N (2018) Effect of nitrogen doping on the pore texture of carbon xerogels based on resorcinol-melamine-formaldehyde precursors. Microporous Mesoporous Mater 256:190–198. https://doi.org/10.1016/j.micromeso.2017.08.004
13. Huber L et al. (2016) Water sorption behavior of physically and chemically activated monolithic nitrogen doped carbon for adsorption cooling. RSC Adv 6(84):80729–80738. https://doi.org/10.1039/C6RA18660B
14. Fu R et al. (2003) The fabrication and characterization of carbon aerogels by gelation and supercritical drying in isopropanol. Adv Funct Mater 13(7):558–562. https://doi.org/10.1002/adfm.200304289
15. Kiciński W, Norek M, Jankiewicz BJ (2014) Heterogeneous carbon gels: N-doped carbon xerogels from resorcinol and N-containing heterocyclic aldehydes. Langmuir 30 (47):14276–14285. https://doi.org/10.1021/la503207t
16. Liu C, Li L, Song H, and Chen X (2007) Facile synthesis of ordered mesoporous carbons from F108/resorcinol–formaldehyde composites obtained in basic media. Chem Commun, 7:757–759. https://doi.org/10.1039/B614199D
17. Iswar S, Malfait WJ, Balog S, Winnefeld F, Lattuada M, Koebel MM (2017) Effect of aging on silica aerogel properties. Microporous Mesoporous Mater 241:293–302. https://doi.org/10.1016/j.micromeso.2016.11.037
18. Sing SW et al. (2008) Reporting Physisorption Data for Gas/Solid Systems. In: Handbook of Heterogeneous Catalysis, Weinheim (Eds), Wiley-VCGVerlag GmbH & Co. KGaA
19. Ahmadpour A, Do DD (1996) The preparation of active carbons from coal by chemical and physical activation. Carbon 34 (4):471–479
20. Martinez-Escandell M, de Castro MM, Molina-Sabio M, Rodriguez-Reinoso F (2013) KOH activation of carbon materials obtained from the pyrolysis of ethylene tar at different temperatures. Fuel Process Technol 106:402–407. https://doi.org/10.1016/j.fuproc.2012.09.005
21. Mohamed AR, Mohammadi M, Darzi GN (2010) Preparation of carbon molecular sieve from lignocellulosic biomass: a review. Renew Sustain Energy Rev 14(6):1591–1599. https://doi.org/10.1016/j.rser.2010.01.024
22. Rodriguez-Reinoso F, Molina-Sabio M (1992) Activated carbons from lignocellulosic materials by chemical and/or physical activation: an overview. Carbon 30(7):1111–1118
23. Okada K, Yamamoto N, Kameshima Y, Yasumori A (2003) Porous properties of activated carbons from waste newspaper prepared by chemical and physical activation. J Colloid Interface Sci 262(1):179–193. https://doi.org/10.1016/S0021-9797(03)00107-3
24. Guo S et al. (2009) Effects of CO2 activation on porous structures of coconut shell-based activated carbons. Appl Surf Sci 255 (20):8443–8449. https://doi.org/10.1016/j.apsusc.2009.05.150
25. Betancur M, Martínez JD, Murillo R (2009) Production of activated carbon by waste tire thermochemical degradation with CO2. J Hazard Mater 168(2–3):882–887. https://doi.org/10.1016/j.jhazmat.2009.02.167
26. This H (2007) Formal descriptions for formulation. Int J Pharmaceutics 344(1–2):4–8. https://doi.org/10.1016/j.ijpharm.2007.07.046
27. This H (2012) Solutions are solutions, and gels are almost solutions. Pure Appl Chem 85(1):257–276. https://doi.org/10.1351/PAC-CON-12-01-01
28. This H (2017) Statgels and dynagels. Notes Académiques de l'Académie d'Agriculture de France (N3AF). vol. 1, p1–12. hal-01637757

29. ISO-15901-3 (2007) Pore size distribution and porosity of solid materials by mercury porosimetry and gas adsorption. Analysis of micropores by gas adsorption. Part 3. https://www.iso.org/obp/ui/#iso:std:40364:en
30. Olivier JP (1995) Modeling physical adsorption on porous and nonporous solids using density functional theory. J Porous Mater 2(1):9–17. https://doi.org/10.1007/BF00486565
31. Olivier JP (1996) The determination of surface energetic heterogeneity using model isotherms calculated by density functional theory. In: MD LeVan (ed) Fundamentals of Adsorption, 356 Springer, US Boston, MA, p 699–707
32. Tarazona P (1985) Free-energy density functional for hard spheres. Phys Rev A 31(4):2672
33. Tarazona P, Marconi UMB, Evans R (1987) Phase equilibria of fluid interfaces and confined fluids: non-local versus local density functionals. Mol Phys 60(3):573–595. https://doi.org/10.1080/00268978700100381
34. Stahl T, Brunner S, Zimmermann M, Ghazi Wakili K (2012) Thermo-hygric properties of a newly developed aerogel based insulation rendering for both exterior and interior applications Energy Build 44:114–117. https://doi.org/10.1016/j.enbuild.2011.09.041
35. Mitsunaga T, Conner AH, Hill CG (2002) Predicting the hydroxymethylation rate of phenols with formaldehyde by molecular orbital calculation. J Wood Sci 48(2):153–158. https://doi.org/10.1007/BF00767293
36. Ren B, Li C, Yuan X, Wang F (2003) Determination and correlation of melamine solubility. J Chem Ind Eng-China 54 (7):1001–1001
37. Okano M, Ogata Y (1952) Kinetics of the condensation of melamine with formaldehyde. J Am Chem Soc 74(22):5728–5731
38. XU P, HUANG L, LI R (2008) Solubility study of melamine in the solution with different pH. Anhui Chem Ind 48(6):23–24
39. Głowacz-Czerwonka D (2013) Prospects of using melamine solutions in reactive solvents in polymer technology. Chemik 67:289–300. https://www.semanticscholar.org/paper/Prospects-of-using-melamine-solutions-in-reactive-G%C5%82owacz-Czerwonka/0dcf57c07a98bd08559574551aad78eef17c6e12
40. Koeda K (1954) Studies on the condensation products of melamine with formaldehyde. I. Analysis of the products composition by paper-chromatographic method. Nippon kagaku zassi 75 (5):571–574. https://doi.org/10.1246/nikkashi1948.75.571
41. Bann B, Miller SA (1958) Melamine and derivatives of melamine. Chem Rev 58(1):131–172. https://doi.org/10.1021/cr50019a004
42. Huber L et al. (2016) Monolithic nitrogen-doped carbon as a water sorbent for high-performance adsorption cooling. RSC Adv 6 (30):25267–25278. https://doi.org/10.1039/C6RA00548A
43. Huber L et al. (2019) The effect of activation time on water sorption behavior of nitrogen-doped, physically activated, monolithic carbon for adsorption cooling. Microporous Mesoporous Mater 276:239–250. https://doi.org/10.1016/j.micromeso.2018.09.025
44. Scherrer P (1912) Bestimmung der inneren Struktur und der Größe von Kolloidteilchen mittels Röntgenstrahlen. In: *Kolloidchemie Ein Lehrbuch*, Springer, Berlin Heidelberg, p 387–409
45. Ayral A, Phalippou J, Woignier T (1992) Skeletal density of silica aerogels determined by helium pycnometry. J Mater Sci 27 (5):1166–1170
46. Llewellyn PL, Rodriquez-Reinoso F, Rouqerol J, Seaton N (2007) Is the BET equation applicable to microporous adsorbents?. Stud Surf Sci Catal 160:49
47. Schneider P, Hudec P, Solcova O (2008) Pore-volume and surface area in microporous–mesoporous solids. Microporous Mesoporous Mater 115(3):491–496. https://doi.org/10.1016/j.micromeso.2008.02.024
48. Rey-Raap N, Angel Menéndez J, Arenillas A (2014) RF xerogels with tailored porosity over the entire nanoscale. Microporous Mesoporous Mater 195:266–275. https://doi.org/10.1016/j.micromeso.2014.04.048
49. Rey-Raap N, Arenillas A, Menéndez JA (2016) A visual validation of the combined effect of pH and dilution on the porosity of carbon xerogels. Microporous Mesoporous Mater 223:89–93. https://doi.org/10.1016/j.micromeso.2015.10.044
50. Lin C, Ritter JA (1997) Effect of synthesis pH on the structure of carbon xerogels. Carbon 35(9):1271–1278. https://doi.org/10.1016/S0008-6223(97)00069-9
51. Taylor SJ, Haw MD, Sefcik J, Fletcher AJ (2014) Gelation mechanism of resorcinol-formaldehyde gels investigated by dynamic light scattering. Langmuir 30(34):10231–10240. https://doi.org/10.1021/la502394u
52. Jelle BP (2011) Traditional, state-of-the-art and future thermal building insulation materials and solutions – properties, requirements and possibilities. Energy Build 43(10):2549–2563. https://doi.org/10.1016/j.enbuild.2011.05.015
53. Kumar KV, Preuss K, Guo ZX, Titirici MM (2016) Understanding the hydrophilicity and water adsorption behavior of nanoporous nitrogen-doped carbons. J Phys Chem C 120(32):18167–18179. https://doi.org/10.1021/acs.jpcc.6b06555